Macroporosity and Grain Density of Rubble Pile Asteroid (162173) Ryugu

Matthias Grott[1], Jens Biele[2], Patrick Michel[3], Seiji Sugita[4], Stefan Schröder[1], Naoya Sakatani[5], Wladimir Neumann[6,1], Shingo Kameda[7], Tatsuhiro Michikami[8], Chikatoshi Honda[9]

[1]German Aerospace Center, Berlin, Germany
[2]German Aerospace Center, Cologne, Germany
[3]Université Côte d'Azur, Observatoire de la Côte d'Azur, CNRS, Laboratoire Lagrange, Nice, France
[4]University of Tokyo, Tokyo, Japan
[5]ISAS/JAXA, Sagamihara, Japan
[6]Klaus-Tschira-Labor für Kosmochemie, Institut für Geowissenschaften, Universität Heidelberg, Heidelberg, Germany
[7]Rikkyo University, Tokyo, Japan
[8]Kindai University, Hiroshima, Japan
[9]University of Aizu, Aizu-Wakamatsu, Japan

Key Points:

- Ryugu's large bulk porosity is distributed between intrinsic boulder microporosity and macroporosity due to void spaces in-between boulders.
- We use the boulder size-frequency distribution as observed on the surface together with mixing models to estimate Ryugu's macroporosity.
- We find that macroporosity is 16±3 %, indicating that Ryugu's large bulk porosity of close to 50 % is governed by microporosity.

Corresponding author: Matthias Grott, matthias.grott@dlr.de

Abstract

Rubble pile asteroids such as (162173) Ryugu have large bulk porosities, which are believed to result from void spaces in between the constituent boulders (macroporosity) as well as void spaces within the boulders themselves (microporosity). In general, both macroporosity and microporosity are estimated based on comparisons between the asteroid bulk density and both the bulk and grain density of meteorite analogues, and relatively large macroporosities are usually obtained. Here we use semi-empirical models for the macroporosity of multi-component mixtures to determine Ryugu's macroporosity based on the observed size-frequency distribution of boulders on the surface. We find that Ryugu's macroporosity can be significantly smaller than usually assumed, as the observed size-frequency distribution allows for an efficient packing of boulders, resulting in a macroporosity of 16±3 %. Therefore, we confirm that Ryugu's high bulk porosity is a direct consequence of a very large boulder microporosity. Furthermore, using estimates of boulder microporosity of around 50 % as derived from in-situ measurements, the average grain density in boulders is 2848±152 kg m^{-3}, similar to values obtained for CM and the Tagish lake meteorites. Ryugu's bulk porosity corresponding to the above values is 58 %. Thus, the macroporosity of rubble pile asteroids may have been systematically overestimated in the past.

Plain Language Summary

The carbonaceous asteroid (162173) Ryugu formed from fragments which re-accreted after its parent body was disrupted by a catastrophic collision. Asteroids of this type are also known as rubble piles and the re-accumulation process is thought to be one of the causes for their large bulk porosity. We have applied mixing models to determine the amount of inter-boulder porosity taking the observed abundance of large and small boulders on the surface into account. We find that the relative abundances of differently sized boulders allow for a very efficient packing, such that inter-boulder porosity in Ryugu is rather small and only 16±3 %. This implies that a large part of Ryugu's total porosity must reside inside the boulders themselves. Using estimates of boulder intrinsic porosity, we furthermore constrain the average density of the boulder's constituent minerals to 2848±152 kg m^{-3}, which is consistent with values measured for carbonaceous meteorites as collected on Earth. Thus, inter-boulder porosity of rubble pile asteroids may have been systematically overestimated in the past.

1 Introduction

Upon arrival of the Hayabusa2 spacecraft the C-complex asteroid (162173) Ryugu was found to be a spinning top-shaped rubble pile (Watanabe et al., 2019) with Cb-type spectrum and very low albedo around 0.045, consistent with thermally metamorphosed CM/CI meteorites (Sugita et al., 2019). Observations further show that a weak 2.7 µm-absorption is present, suggesting a small amount of hydrated minerals exist on the surface (Kitazato et al., 2019). Furthermore, the surface was found to be dominated by blocks and boulders (Sugita et al., 2019; Michikami et al., 2019), and 50% of the surface is covered by boulders with diameters exceeding 0.5 m. A bulk density of 1190±20 kg m^{-3} was determined using the SFM20180804 shape model (Watanabe et al., 2019), which allowed for an estimate of asteroid porosity. Assuming typical grain densities for carbonaceous chondrites (Britt & Consolmagno S.J., 2001; Macke et al., 2011; Flynn et al., 2018), bulk porosity estimates close to 50 % were obtained (Watanabe et al., 2019), which is consistent with the bulk porosity estimates for C-complex asteroids.

The bulk porosity inside rubble pile asteroids can be separated into two contributions: the first one stems from the intrinsic porosity of rocks and boulders and is termed microporosity, while the second contribution refers to voids in-between particles and is termed macroporosity (Britt et al., 2002). The latter is directly related to the geometrical arrangement of the constituent blocks, also known as the packing state, which qualitatively describes the arrangement of particles and can vary between random loose and random close packings. Macroporosity of average C-complex asteroids was estimated to be 25-30 % (Britt et al., 2002), which is generally consistent with numerical models of the reassembly of blocks after a catastrophic disruption, which result in macroporosities of 20-40 % (Wilson et al., 1999). However, simulations suffer from unrealistically large lower cutoff sizes for the considered boulder population, such that rubble pile asteroids may still exhibit lower macroporosities.

Here we investigate the macroporosity of asteroid Ryugu using semi-empirical models for the porosity of multi-component mixtures of non-spherical, cohesive particles (Zou et al., 2011). Such models predict the macroporosity of granular material given the particle size as well as the particle shape distributions applying linear mixing and using the concept of controlling mixtures (Yu & Standish, 1991) to calculate the packing state. In general, polydisperse particle mixtures can have a macroporosity which is considerably

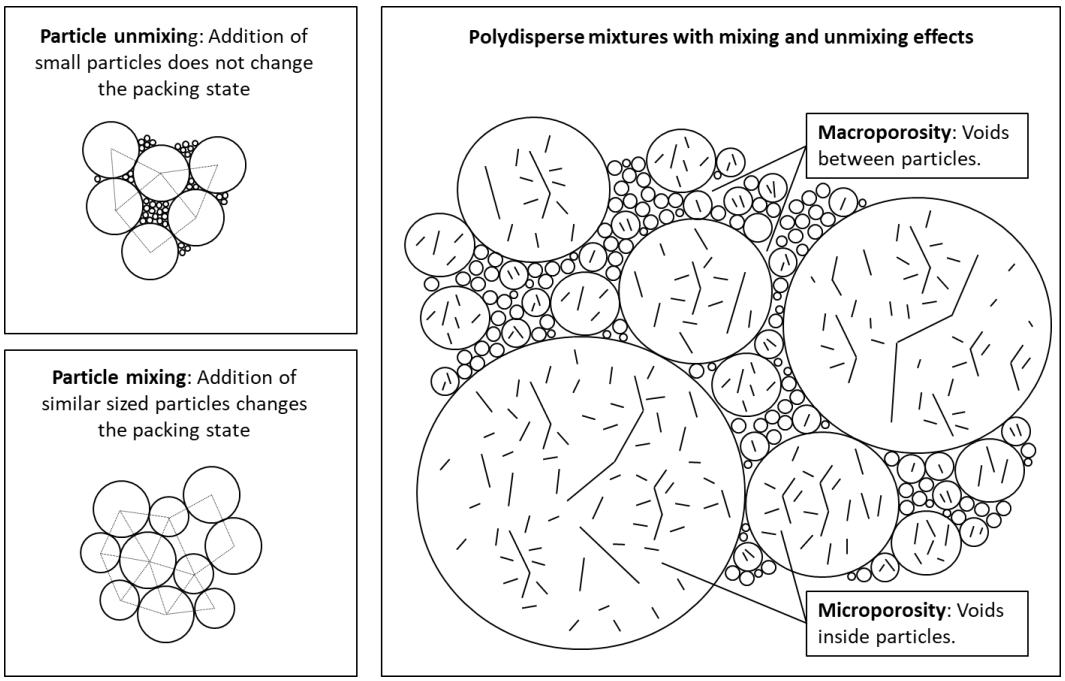

Figure 1. Top Left: Illustration of particle unmixing for particles with strongly disparate diameters. As small particles are added to a system of larger particles, the larger particles resist being displaced and the packing state does not change. A similar effect occurs for the addition of very large particles. Bottom Left: Illustration of particle mixing for particles with similar diameters. As similar sized particles are added to a system, particles can be displaced thus changing the packing state. Right: Two dimensional illustration of the random packing structure of strongly polydisperse spheres. As compared to monodispersed configurations, porosity is reduced by the filling of void spaces. Macroporosity refers to the porosity generated by the void spaces between particles, while microporosity is caused by void spaces and cracks that formed inside individual particles. Figure adapted from Yu & Zou (1998).

smaller than the canonical ∼36 % for a random close packing or ∼42 % for a random loose packing of spherical, monosized particles (Scott, 1960), and values down to 10 % can be reached (Dullien, 1991).

In binary mixtures, the way particles interact depends on their size ratio, here defined as the ratio of the respective particles' volume-equivalent diameters. If this ratio is less than 0.154 (Graton & Fraser, 1935), small particles will not affect the packing state and simply fill the gaps between larger ones. In contrast to this unmixing of particles, similar sized particles will mix, creating a new packing structure (also see Yu & Zou (1998) for a discussion of mixing and unmixing effects). Applying these concepts to polydisperse mixtures, particle unmixing will take place for very small and very large particles, as smaller particles start filling the gaps and larger particles completely fill some regions with solid material. The component controlling the porosity of the mixture is then defined by intermediate sized particles, which do not change their packing state by the addition of unmixing components (Yu & Zou, 1998). An illustration of particle mixing and unmixing is shown in Fig. 1. The semi-empirical models by Yu & Zou (1998) and Zou et al. (2011) can be applied to particle mixtures in loose and dense packing states. They have been shown to reproduce the porosity of mixtures created using the funnel method, in which particles are gently poured into a container, as well as the porosity of mixtures tapped many times to reach maximum compaction.

It is important to note that packing is determined by the interplay of the different grain sizes present, and it can be misleading to consider individual grain sizes only. For example, while the addition of a single large block to the mixture can reduce porosity by displacing smaller particles and filling void spaces, the addition of many large blocks can increase porosity by creating large voids. Similarly, addition of some small particles may reduce porosity, while many small particles can create a large number of small voids, again increasing porosity. Therefore, the porosity finally attained by the mixture depends on the details of the size-frequency distribution of the particles present.

In order to apply the theory of multi-component mixtures, the size and shape distributions of boulders need to be known. Here we use the boulder size and shape distributions determined by Michikami et al. (2019), who extend the analysis in Sugita et al. (2019) using images from the Hayabusa2 optical navigation camera (ONC) (Kameda et al., 2017; Suzuki et al., 2018; Tatsumi et al., 2019) which have near global coverage

and were acquired at altitudes between 20 km and 6.5 km. These have spatial resolutions down to 0.65 m/pixel, and global counts were performed for boulders with diameters > 2 m and a completeness limit of 5 m. In addition, smaller boulders, cobbles and pebbles with sizes of 0.02 to 9.1 m were studied using close-up images of the sampling areas, where images taken at altitudes from 67 m to 620 m with resolutions down to $<$ 0.01 m/pixel are available (Michikami et al., 2019). Overall, size-frequency and shape distributions were determined in the 0.02 to 140 m size range.

By applying the multi-component mixing model to the size distribution of boulders as observed on the surface, we assume that the same distribution holds in the interior. This assumption is supported by laboratory experiments on the disruption of monoliths (Michikami et al., 2016), which suggest that boulders on bodies such as Itokawa, Bennu, and Ryugu are relicts of the direct formation of those asteroids by gravitational reaccumulation following the disruption of their parent bodies (Michel & Richardson, 2013; Michel et al., 2020) rather than the result of impact events after formation has been completed. Impacts could reshape the size distribution by the production of smaller particles after reaccretion has been completed, but the importance of this process may be limited. This is due to the so-called armoring effect (Sugita et al., 2019), by which a large fraction of the impact energy is lost when the projectile contacts the first large boulder, thus producing only few fragments. Another mechanism that could be responsible for a difference between the size-frequency distributions observed on the surface and present in the interior is seismic shaking, and the Brazil Nut Effect could lead to an overrepresentation of large boulders on the surface (Tancredi et al., 2015; Maurel et al., 2017). However, the seismic efficiency of impacts in granular material appears to be low (Yasui et al., 2019; Nishiyama et al., 2020), such that surface modifications are likely localized. Nevertheless, seismic shaking could have an impact on the global boulder size-frequency distribution over geological timescales. Finally, it has been argued that particle size sorting may take place during rubble pile reaccretion, with larger blocks accreting first and thus in the center (Britt & Consolmagno S.J., 2001). These caveats need to be kept in mind when interpreting the results presented below.

A second important input parameter for the multi-component mixing model is the material's packing state, which can vary between a random loose and random close packing. In general, little is known about the packing state of rubble pile asteroids following reaccretion, which depends on many parameters such as the distribution of angu-

lar momentum in the reaccreting system as well as the size distribution and shape of reaccreting fragments. While impact experiments indicate that shattered, elongated particles with large deviations from a spherical shape can be produced (Nakamura & Fujiwara, 1991; Durda et al., 2015; Michikami et al., 2016) the results of disruption experiments need to be interpreted with caution, as the high strain rates imposed during the experiment may not be representative for the destruction of larger blocks. Further, long term seismic shaking could lead to the reduction of pore spaces. Given these unknowns, we will systematically vary the packing state in the analysis below.

In the following, we will first introduce the theory of determining asteroid macroporosity from observed size and shape distributions for the rocks and boulders. We will then derive a simple equation relating grain density to macro- and microporosity. Results of the macroporosity calculation and relevant uncertainties will then be used to estimate grain density of Ryugu's constituent material given estimates of boulder microporosity (Grott et al., 2019; Hamm et al., 2020; Okada et al., 2020). Finally, results, assumptions, and implications will be discussed.

2 Methods

2.1 Particle Size and Shape Distributions

To estimate Ryugu's macroporosity, the constituent boulder's size and shape distributions need to be known. These were determined by Michikami et al. (2019) who fitted size-frequency data using power laws. Power law exponents between 1.65 and 2.65 were obtained, with 2.65 being the best fit for the global dataset. Furthermore, particles were generally found to be elongated, and axis ratios for boulders > 2 m are close to 0.7 on average. The size-frequency distribution of boulders on small bodies may better be described by a Weibull distribution than a power law (Schröder et al., 2020), and we have used a cumulative Weibull (Rosin-Rammler) distribution (Rosin, 1933; Weibull, 1951; Wingo, 1989; Brown & Wohletz, 1995) to represent the data provided by Michikami et al. (2019). The cumulative size-frequency distribution $N(D)$ is then given by

$$N(D) = N_T e^{-3(D/\lambda)^\beta/\beta} \tag{1}$$

where D is the mean horizontal diameter, and we determined the fit parameters $\beta = 0.09495$, $\lambda = 33.78$ m, and $N_T = 5.28 \cdot 10^{14}$ km^{-2} by a weighted least-squares approach as a practical means to obtain a good representation of the data. The resulting

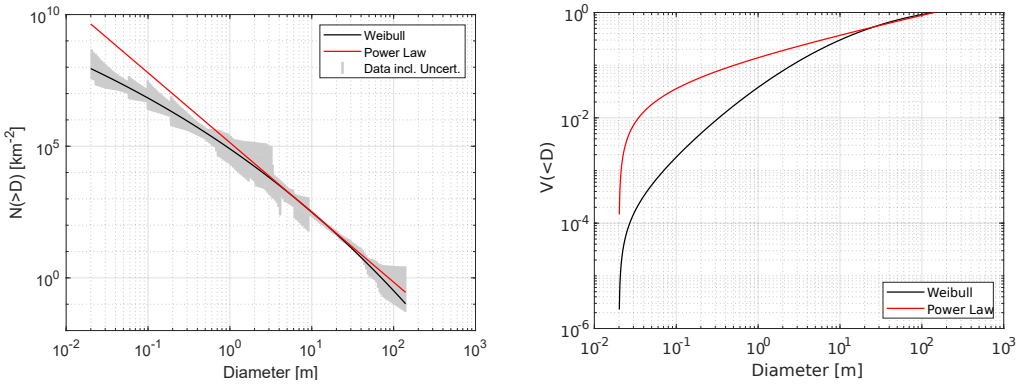

Figure 2. Left: Cumulative particle size frequency distribution (SFD) as derived for Ryugu by Michikami et al. (2019). Our Weibull fit to the data (black) is shown along with a power law fit with exponent $p = 2.65$ (red). Right: Cumulative volume fraction distribution for the SFDs on the left hand side of the figure.

distribution $N(D)$ is shown together with the uncertainty of the data in Fig. 2, where uncertainty comprises the Poisson uncertainty as well as the uncertainty of particle diameters introduced by the limited image resolution. It is worth noting that representing the data using a single power law for the entire size range does not adequately represent the data.

Given the size-frequency distribution $N(D)$ as determined from surface counts of boulders, the normalized cumulative volume distribution $V(D)$ can be calculated by numerical integration. It is given by

$$V(D) = c\left(N_{\mathrm{tot}} D_{\mathrm{min}}^3 - N(D)D^3 + \int_{D_{\mathrm{min}}}^{D} N(D')3D'^2 dD'\right) \tag{2}$$

where N_{tot} is the total number of particles counted per unit area, D_{min} and D_{max} are the minimum and maximum particle sizes of the particle size distribution $N(D)$, respectively, and c $[\mathrm{m}^{-1}]$ is a normalization factor chosen such that $V(D_{\mathrm{max}}) = 1$.

In addition to the Weibull distribution fit to the data represented by Eq. 1, we will also consider a simple power law to systematically study the influence of the particle size distribution's power law exponent p on the obtained results. The distribution can then be expressed as

$$N(D) = N_{\mathrm{tot}}\,(D/D_{\mathrm{min}})^{-p} \tag{3}$$

where $p = 2.65$ represents the best fit to the global dataset (Michikami et al., 2019). For the power law defined by Eq. 3, Eq. 2 can be integrated analytically and the volume size distribution is then given by

$$V(D) = \frac{D^{3-p} - D_{\min}^{3-p}}{D_{\max}^{3-p} - D_{\min}^{3-p}} \tag{4}$$

for $D_{\min} \leq D \leq D_{\max}$. For $D \geq D_{\max}$, $V(D) = 1$, whereas for $D \leq D_{\min}$ $V(D) = 0$.

Michikami et al. (2019) give the shape of boulders in terms of the maximum dimensions in three mutually orthogonal planes ($a \geq b \geq c$). Here we primarily regard the horizontal axis ratio b/a, with a being the maximum and b the intermediate dimension. As reported by Michikami et al. (2019), shape of particles on Ryugu appears to be largely independent of geographical longitude, whereas some dependence on latitude may indicate boulder migration. Nevertheless, average b/a is only weakly size-dependent and close to 0.7.

In general, particle sphericity is defined as the ratio of the surface area of a sphere (with the same volume as the particle) to the surface area of the particle (Wadell, 1932). However, this is difficult to evaluate in practice, and the Krumbein (Krumbein, 1941) or Riley (Riley, 1941) simplifications are usually applied. Working with two dimensional (image) data, we define sphericity Ψ as

$$\Psi = \sqrt{\frac{D_i}{D_c}} \tag{5}$$

where D_i is the diameter of the largest inscribed circle and D_c is the diameter of the smallest circumscribing circle for a given particle (Riley, 1941). Using Eq. 5, the shape parameter b/a derived by Michikami et al. (2019) then translates into an average sphericity of $\Psi = 0.83$. In addition, Michikami et al. (2019) also estimated the third axis, c/a, of 121 arbitrarily selected boulders. The mean axes ratio c/a was found to be 0.44, and the sphericity of a parallelepiped with axis ratios a:b:c of 1:0.71:0.44 is 0.796. On the other hand, sphericity of a triaxial ellipsoid with the same axis ratios is 0.913. Therefore, sphericity depends not only on axis ratios, but also on particle shape, and we will use $\Psi = 0.85 \pm 0.06$ as an average sphericity rather than the average sphericity derived from the shape data in Michikami et al. (2019) when calculating interparticle forces and initial porosities below.

2.2 Macroporosity

The macroporosity of Ryugu can be calculated from the volume size-frequency distribution (Eq. 2) assuming linear mixing models (Yu & Zou, 1998; Zou et al., 2011). In the mixing theory, the macroporosity achieved for a given size distribution will be a function of the volume fractions X_i, the initial porosity ϕ_i, as well as the nominal equivalent volume diameter d_i of particles in each bin. The latter represents the diameter of a volume-equivalent sphere. Further, $i = 1, \ldots, n$ is the number of size bins used and $d_1 > d_2 > \ldots d_n$ for convenience. Then, the macroporosity ϕ_{Macro} can be expressed as

$$\phi_{Macro} = f(X_1, \ldots, X_n; d_1, \ldots, d_n; \phi_1, \ldots, \phi_n). \tag{6}$$

Note that the equivalent volume diameter d_i of particles is not strictly identical to the mean horizontal diameter as defined by Michikami et al. (2019), but as the observed boulder axis ratios on Ryugu change only little as a function of horizontal diameter, the shape factor relating horizontal diameter to the equivalent volume diameter d_i is close to constant. It can thus be factored out for the mixing model below and has a negligible effect on the Bond number.

The above formulation holds if particle sphericity is independent of particle size, which is the assumption made in the following. However, we note for completeness that the method to estimate macroporosity used here can be generalized to arbitrary sphericity-size relations $\Psi(d)$ by introducing the equivalent packing diameter d_p, which then accounts for particle shape effects, i.e., mixing of particles that have different sphericities at different sizes. Then, the equivalent volume diameter d in Eq. 6 needs to be replaced by the equivalent packing diameter d_p, which is related to the observed equivalent volume diameter d through sphericity $\Psi(d)$ by (Yu & Zou, 1998) by the empirical relation

$$\frac{d}{d_p} = \Psi(d)^{2.785} e^{2.946(1-\Psi(d))} \tag{7}$$

The dimensionless specific volume describing the packing state for each bin is defined as (Zou et al., 2011)

$$V_j = \frac{1}{1-\phi_j} \tag{8}$$

and the macroporosity finally attained by the mixture will be governed by the interaction of all differently sized particles. However, there will be one intermediate-sized bin

i that controls the packing structure (see Yu & Zou (1998), also compare Fig. 1). While the size-bin number i of the controlling component is not known a priori, the specific volume $\tilde{V_i}$ of a particular packing can in general be expressed as

$$\tilde{V_i} = \sum_{j=1}^{i-1}[V_j - (V_j - 1)g(d_i, d_j)]X_j + V_i X_i + \sum_{j=i+1}^{n}[V_j(1 - f(d_i, d_j)]X_j \tag{9}$$

where small particles have indices $j = 1 \ldots i-1$ and large particles have indices $j = i{+}1 \ldots n$. The functions $f(d_i, d_j)$ and $g(d_i, d_j)$ are referred to as interaction functions between components i and j and were derived experimentally (Yu et al. (1997), Zou et al. (2011)). They are given by

$$f(d_i, d_j) = f(r_{ij}) = (1 - r_{ij})^{3.33} + 2.81 r_{ij}(1 - r_{ij})^{2.77} \quad \text{and} \tag{10}$$

$$g(d_i, d_j) = g(r_{ij}) = (1 - r_{ij})^{1.97} + 0.36 r_{ij}(1 - r_{ij})^{3.67} \tag{11}$$

and depend on the equivalent packing diameter size ratios r_{ij} between small and large particles of the two components. Parameters r_{ij} can be expressed as (Zou et al., 2011)

$$r_{ij} = (1 - x_{ij})R_{ij}^k + x_{ij} R_{ij} \tag{12}$$

where $R_{ij} = d_j/d_i$ is the small-to-large size ratio and $i < j$. The empirical parameter k is 0.451 (Zou & Yu, 1996), and x_{ij} depends on the type of particle-particle interaction (Zou et al., 2011). It is given by

$$x_{ij} = \begin{cases} 1 & d_j > d_{cri} \\ 0 & d_i < d_{cri} \\ 1 - 1.543 \cdot e^{-0.697 d_i/d_{cri}} & d_j \leq d_{cri} \leq d_i \end{cases} \tag{13}$$

In the above equation, the critical particle diameter d_{cri} divides fine and coarse particles, i.e., it is the particle diameter below which cohesion between particles starts to influence particle interactions. Under Earth gravity conditions, d_{cri} is close to 150 µm (Zou et al., 2011), but under micro-gravity conditions, cohesion can be relevant even for decimeter-sizes boulders (Scheeres et al., 2010; Kiuchi & Nakamura, 2015; Zou et al., 2011). Here, we define the critical diameter based on the Bond number B, i.e., the ratio between interparticle forces and the weight of a particle (Scheeres et al., 2010).

We define the Bond number assuming a cleanliness factor equal to unity and a particle separation of $1.5{\cdot}10^{-10}$ m (Scheeres et al., 2010). Furthermore, we calculate the co-

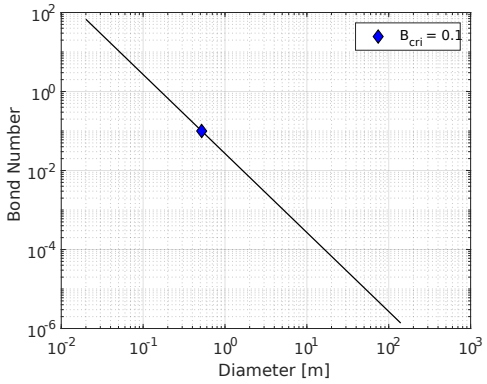

Figure 3. Bond number, i.e., the ratio between interparticle forces and particle weight, as a function of particle diameter, assuming parameters as appropriate for Ryugu. The diameter corresponding to a critical Bond number of $B_{cri} = 0.1$ is indicated.

hesive force for equally sized particles and include effects of particle sphericity Ψ and roundness Ω (Powers, 1953) by adding these as multiplicative factors (Wood, 2020). The Bond number is then given by

$$B(d) = \frac{1.1 \cdot 10^{17} A \Psi \Omega}{\rho g (d/2)^2} \tag{14}$$

where d is particle diameter, $g = 0.9825 \cdot 10^{-4}$ m s^{-2} is volume averaged gravity of Ryugu (Yamamoto et al., 2020), and $A = 4.1 \cdot 10^{-20}$ J is the Hamaker constant for olivine in high vacuum (Perko et al., 2001). While olivine is certainly not the most common mineral in carbonaceous material, we consider its Hamaker constant to be a more appropriate choice than, e.g., the widely used Hamaker constant for amorphous SiO_2. In any case, the Hamaker constant needs to be regarded as highly uncertain. This also implies that the exact choice of parameters like boulder density, sphericity, and roundness has little influence on the results presented below. We choose boulder bulk density $\rho = 1420$ kg m^{-3} to match a macroporosity of 16 % and a bulk density of 1190 kg m^{-3} (Watanabe et al., 2019) for consistency, where ρ was determined using an iterative approach. Furthermore, we choose a particle roundness Ω of 0.24, as appropriate for angular to subangular particles (Powers, 1953).

The resulting Bond number for parameters appropriate for Ryugu is shown in Fig. 3 as a function of particle diameter. The critical diameter d_{cri} corresponding to a critical Bond number $B_{cri} = 0.1$ is indicated in blue and has been calculated using Eq. 14. We use $B_{cri} = 0.1$ as a baseline, i.e., we assume that cohesion starts to have a notice-

able effect on porosity once the interparticle forces exceed 10 % of the particle weight. For Ryugu, $B_{cri} = 0.1$ corresponds to $d_{cri} = 0.52$ m, but the influence of varying B_{cri} over a large range will also be discussed.

To evaluate Eq. 9, we first discretize the size range between $D_{\min} = 0.02$ m and $D_{\max} = 140$ m into $\log(D_{\max}/D_{\min})/\log(q)$ logarithmically spaced bins. We use a size factor of $q = 1.05$ from one bin to the next, resulting in a total of 182 size bins, which turned out to be sufficient. Volume fractions X_i in each size-bin were calculated according to the Weibull or power law representation of the size-frequency distribution as needed. Furthermore, initial specific volumes V_i and therefore initial porosities ϕ_i need to be prescribed. While initial porosities of coarse monosized spherical particles generally vary between 0.42 for loose random packing and 0.36 for dense random packing (Scott, 1960), cohesive forces between small particles can considerably increase porosities (Scheeres et al., 2010; Kiuchi & Nakamura, 2015). We use the empirical relation (Kiuchi & Nakamura, 2015; Kiuchi & Nakamura, 2015b)

$$\phi_i = \phi_0 + (1 - \phi_0)e^{-\alpha B(d_i)^{-\gamma}} \tag{15}$$

to determine initial porosity, where ϕ_0 is the porosity of the non-cohesive particles and describes the packing state. Note that we here implicitly assume initial porosities as appropriate for spherical particles, as for the relevant range of observed sphericities the influence of deviations from an ideal spherical shape on initial porosity is negligible (Zou & Yu, 1996). Particle shape enters Eq. 15 in the Bond number $B(d_i)$ only, and it is a secondary effect in the analysis presented for Ryugu below. The constants $\alpha = 2.414$ and $\gamma = 0.1985$ have been derived from a new fit to the data of Kiuchi & Nakamura (2015). Finally, the specific volume occupied by the mixture is obtained by calculating the maximum of all specific volumes for the different controlling mixture sizes and

$$V = \max\{\tilde{V_1}, \ldots, \tilde{V_n}\} \tag{16}$$

Mixture macroporosity is then given by $\phi_{Macro} = 1 - 1/V$.

In summary, the following steps need to be performed to determine the macroporosity of a granular mixture using the model above: First, volume fractions in the individual size-bins need to be calculated from the given size-frequency distribution (Eq. 8, 9). Then, initial porosity in each size-bin needs to be determined. This will primarily depend on the packing state. Further, it also depends on particle roundness and shape,

which influence cohesion (Eq. 14, 15) as well as the geometrical packing properties (not considered here). Finally, the macroporosity is determined by examining all possible particle interactions (Eq. 16).

2.3 Average Grain Density

While the main goal of the present paper is a determination of the macro-porosity of rubble-pile asteroid Ryugu, additional information on the asteroid's average grain density can be derived. As macroporosity ϕ_{Macro}, microporosity ϕ_{Micro}, and bulk density ρ_{Bulk} are related by

$$\phi_{\mathrm{Macro}} = 1 - \frac{1 - \phi_{\mathrm{Bulk}}}{1 - \phi_{\mathrm{Micro}}} \tag{17}$$

information on grain density ρ_{Grain} can be extracted from

$$\phi_{\mathrm{Bulk}} = 1 - \frac{\rho_{\mathrm{Bulk}}}{\rho_{\mathrm{Grain}}} \tag{18}$$

Eq. 18 requires the macroporosity, microporosity, and bulk density to be known. While the bulk density of Ryugu was estimated to be 1190±20 kg m^{-3} (Watanabe et al., 2019), the boulders' microporosity cannot currently be unambiguously constrained due to the difficulties associated with extrapolating meteorite thermal conductivities to porosities in excess of 20 % (Grott et al., 2019; Macke et al., 2011). However, end-member models (Flynn et al., 2018; Henke et al., 2016) suggest microporosities ϕ_{Micro} of either 32 ± 2 % or 50 ± 2 % for Ryugu's dark and rugged boulders (Hamm et al., 2020) which comprise the vast majority of all boulders observed on the surface (Sugita et al., 2019; Okada et al., 2020). We will use Monte-Carlo simulations to propagate these uncertainties to the determination of Ryugu's grain density, while simultaneously taking the uncertainty associated with Ryugu's macroporosity as derived from the linear mixing theory (Sec. 2.2) into account.

3 Results

Given the parameterization of the size-frequency distribution (Eq. 1) for the boulders observed on the surface of Ryugu, and assuming the distribution also applies to the interior, we have first calculated the corresponding volume frequency distribution using Eq. 2. Given roundness Ω, Hamaker constant A, particle bulk density ρ, and volume average gravity g (see Eq. 14), we then varied the initial porosity ϕ_i in each size bin (Eq.

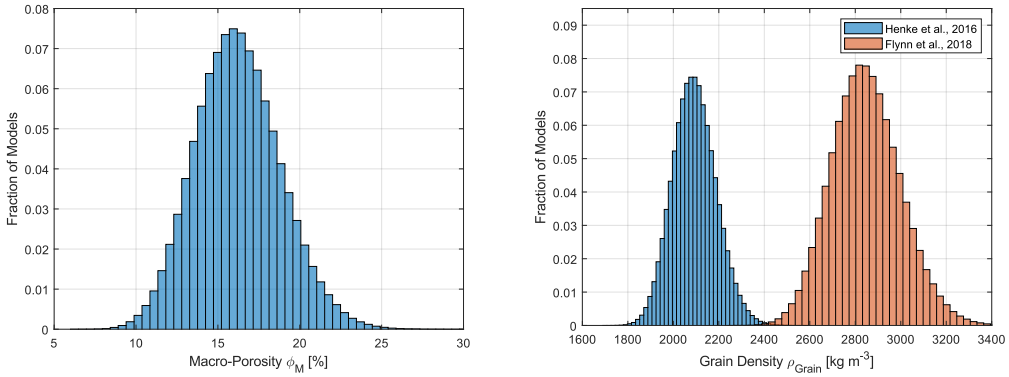

Figure 4. Left: Histogram of macroporosities ϕ_M obtained using Monte-Carlo simulations. Right: Ryugu grain densities derived from a second set of Monte-Carlo calculations (see text for details). The two distinct distributions result from the uncertainty of microporosity for Ryugu's boulders (Grott et al., 2019; Hamm et al., 2020), and two end-member models for the microporosity have been assumed.

15) using a Gaussian distribution for ϕ_0 centered around 39.5 % with standard deviation of 3 %. In addition, particle sphericity was varied using a Gaussian distribution centered around 0.85 with standard deviation of 0.06, and 10^6 draws from these distributions were used in a Monte-Carlo simulation to calculate the resulting macroporosity according to Eq. 16.

Results of the calculation are shown in the left hand panel of Fig. 4, where a histogram of the obtained macroporosities ϕ_M is shown. The range of macroporosities obtained in the calculations is $\phi_M = 16.2 \pm 2.6$ % (1-sigma), and thus considerably smaller than porosities of monodisperse packings. This is not surprising given the broad particle size distribution observed on the surface of Ryugu.

Given the range of macroporosities derived above as well as estimates for the boulder microporosities derived from in-situ thermal inertia measurements (Grott et al., 2017, 2019; Hamm et al., 2020), we calculated the range of grain densities compatible with the observed bulk porosity of Ryugu (Watanabe et al., 2019) using Eq. 17 and 18. We applied two endmember models for the microporosity ϕ_{Micro}: for the first model (Flynn et al., 2018) we use $\phi_{Micro} = 50 \pm 2$ %, while for the second model (Henke et al., 2016) $\phi_{Micro} = 32 \pm 2$ % (Hamm et al., 2020). In the 10^6 Monte-Carlo simulations performed, we varied microporosity using Gaussian distributions centered around 50 % and 32 %

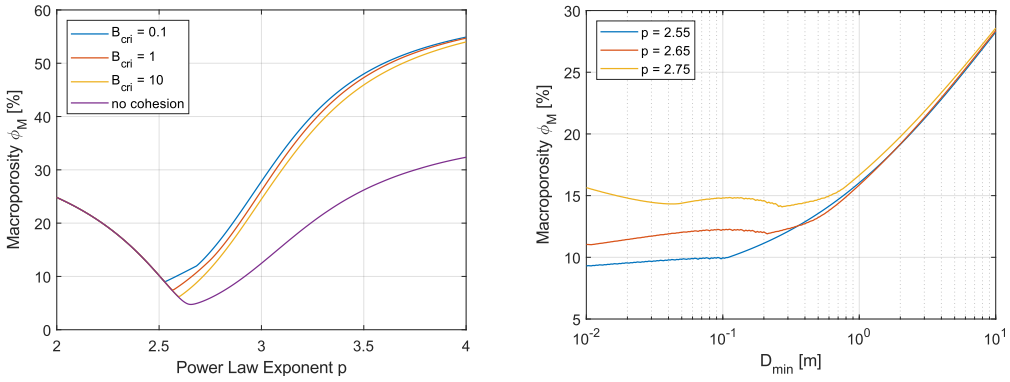

Figure 5. Left: Macroporosity ϕ_{Macro} (porosity caused by void spaces in-between particles) as a function of the power law exponent of the underlying size-frequency distribution and critical Bond number B_{cri}. For comparison, results obtained neglecting cohesion between particles are also shown. Right: Macroporosity ϕ_{Macro} as a function of lower cutoff size D_{min} for three different power law exponents p. For reference, the power law exponent for Ryugu as derived from the observed surface boulder size-frequency distribution is $p = 2.65$ on average (Michikami et al., 2019).

with standard deviations of 2 %, respectively. Furthermore, we varied bulk density using a Gaussian distribution centered around 1190 kg m^{-3} with a standard deviation of 20 kg m^{-3} (Watanabe et al., 2019) and macroporosity using a Gaussian distribution centered around 16.2% with a standard deviation of 2.6 %.

Results of the calculation are shown in the right hand panel of Fig. 4, where the resulting histograms for the grain densities ρ_{Grain} are shown for the two endmember models. Owing to the two different models used to estimate boulder microporosity, two separate peaks are obtained for the distribution of grain densities. For the model of Flynn et al. (2018), we find grain densities of $\rho_{Grain} = 2848 \pm 152$ kg m^{-3}, whereas the model of Henke et al. (2016) results in $\rho_{Grain} = 2093 \pm 96$ kg m^{-3}. As expected, higher microporosities (Flynn et al., 2018) yield larger grain densities and vice versa to satisfy the constraint posed by Ryugu's bulk density.

Results of a systematic study of the influence of critical Bond number B_{cri} and lower diameter cutoff sizes $D_{\min}$ on the obtained macroporosities ϕ_{Macro} are shown in Fig. 5. Here, the size-frequency distribution of boulders has been approximated by a power law with exponent p to facilitate a comparison of Ryugu with other rubble pile asteroids. For

smaller power law exponents, the size-frequency distribution is shallower as compared to distributions with larger p, and as a result, such distributions represent surfaces with a higher ratio of large particles.

In general, the macroporosities ϕ_{Macro} obtained using the above mixing theory show a distinct minimum at intermediate power law exponents p, whereas distributions which have too many small or too many large particles result in unfavorable mixing and larger ϕ_{Macro} are obtained. This minimum around $p = 2.5$ is known as the Fuller parabola in the engineering literature and has long been known as the optimum packing size distribution for spherical particles (Fuller & Thompson, 1907). Results obtained varying the critical Bond number are shown in the left panel of Fig. 5, where the critical Bond number parametrizes the particle size below which interparticle forces result in significant cohesion. As expected, low critical Bond numbers, corresponding to larger contributions from cohesive particles, result in larger macroporosities. However, the overall effect is small and in the few percent range. The low critical Bond number of 0.1 adopted above therefore results in a conservative upper limit on macroporosity. It is also worth noting that results obtained using a power law distribution with $p = 2.65$, which overestimates the fraction of small particles, are lower than those obtained using the Weibull representation of the data by 4-5 %, such that results obtained using global power law fits must be interpreted with caution. For comparison, results obtained neglecting cohesion are also shown in the left panel of Fig. 5, and macroporosity approaches a limit of 39.5 % (compare Eq. 15) for large p (not shown).

The influence of varying the lower cutoff diameter $D_{\min}$ of the size-frequency distribution on the obtained macroporosity ϕ_{Macro} is shown in the right panel of Fig. 5, where ϕ_{Macro} is shown as a function of $D_{\min}$ for three power law exponents p. In the calculations, a critical Bond number of $B_{cri} = 0.1$ has been assumed. While the minimum macroporosity that can be achieved by the packing is close to constant for small D_{min}, predicted macroporosity drastically increases for cutoff diameters larger than a few decimeters. In this case, unfavorable mixing is a result of the sparsity of smaller rocks to fill the gaps between larger blocks. These results indicate that image data with centimeter resolution are necessary to properly characterize the packing state of rubble pile asteroids, and that results presented above are largely independent of the cutoff size of $D_{\min} = 0.02$ m imposed by the image data available for Ryugu.

4 Discussion and Conclusions

In the present paper, we have used semi-empirical models for the porosity of multi-component mixtures to estimate the macroporosity of Cb-type asteroid (162173) Ryugu based on the observed size-frequency distribution of boulders on the asteroid's surface and the assumption that the surface distribution of boulders is representative for the bulk asteroid. Using the concept of controlling mixtures (Yu & Standish, 1991; Yu & Zou, 1998; Zou et al., 2011), we estimated the macroporosity of Ryugu to be $\phi_M = 16.2 \pm 2.6$ %. Based on estimates of boulder microporosity, we furthermore constrained the average grain density of Ryugu's boulders to $\rho_{Grain} = 2848 \pm 152$ kg m^{-3} or $\rho_{Grain} = 2093 \pm 96$ kg m^{-3}, depending on the microporosity model used.

Boulder shape can affect the above mixing model by changing interparticle cohesion, by changing the geometrical arrangement between different particle sizes, and by changing the initial porosity in each individual size-bin. In the modeling, we have taken the influence of shape on particle cohesion explicitly into account, while we neglected its influence on geometrical interactions and initial porosity. This is justified because for the case of Ryugu **the majority of particles have axis ratios b/a** in excess of 0.5 (Michikami et al., 2019), corresponding to sphericities larger than 0.7. For such particles, initial porosity is nearly independent of shape and equal to the value appropriate for spherical particles (Zou & Yu, 1996). It is also worth noting that for Ryugu all of the above are secondary effects when compared to the unknown packing state, which we address by considering the entire range stretching from a random loose to a random close packing.

For the case of Ryugu, the primary factor determining macroporosity is the boulder size-frequency distribution, and while the applied model takes cohesion between particles into account, disregarding cohesion results in only a slight modification of the obtained macroporosity ϕ_M. Switching off cohesion in the model by assuming a critical bond number of 10^5 results in a macroporosity of 16.1 %, only 0.1 % smaller than the value presented above. This is a direct consequence of the low volume fraction of small cohesive particles on Ryugu, which directly follows from the given boulder size-frequency distribution. This also implies that the results presented here are robust with respect to the exact choice of parameters like boulder density, roundness, and sphericity, which enter the calculation of the Bond number. It is also worth noting that the power law representation of the data significantly overestimates the influence of cohesion on macro-

446 porosity when compared to the Weibull fit by overestimating the volume fraction of small
447 particles.

448 The cratering experiment performed by Hayabusa2's small carry-on impactor re-
449 sulted in the formation of a crater in the gravity-dominated regime (Arakawa et al., 2020),
450 indicating that particle cohesion played a minor role in the crater formation process. On
451 the other hand, particles with diameters of 0.2 m were observed in the SCI crater wall,
452 which, according to Eq. 14, have Bond numbers close to unity and should therefore in-
453 teract cohesively. This apparent discrepancy is resolved by the fact that small particles
454 appear not to be volumetrically dominant inside Ryugu. This is indicated by the shal-
455 low particle size distribution for particles smaller than 1 m on the surface (Sugita et al.,
456 2019; Michikami et al., 2019) and inside the artificial crater (Arakawa et al. (2020), Fig.
457 S5), where the particle size distribution shows a power law exponent $p \sim 2$ (also com-
458 pare the volume-size distribution on the right hand side of Fig. 2). Therefore, results of
459 the cratering experiment confirm that cohesion has a small influence on Ryugu's pack-
460 ing state. However, cohesion may become significant for rubble pile asteroids with a steep
461 particle size distribution, e.g., power-laws with $p > 3$, where - in contrast to Ryugu -
462 the mixture is dominated by a high volume fraction of very small particles.

463 Although a full analysis using empirical fits of the cumulative boulder size-frequency
464 distribution of other small bodies has not been performed here, macroporosity results
465 can be qualitatively compared by considering the power law exponents of their respec-
466 tive size distributions and assuming similar size cutoffs $D_{\min}$ and $D_{\max}$. The former have
467 been widely used to describe size distributions in the literature, and values of $p = 2.9\pm$
468 0.3 and $p = 3.52\pm0.20$ have been obtained for Bennu (Lauretta et al., 2019) and Itokawa
469 (Michikami et al., 2008; Mazrouei et al., 2014; Michikami et al., 2019), respectively. As-
470 suming $B_{cri} = 0.1$ as above, these correspond to macroporosities between 10 and 38 %
471 for Bennu and 43 to 52 % for Itokawa. Assuming average grain densities of 2600 kg m^{-3},
472 Bennu's low bulk density of 1190±13 kg m^{-3} (Lauretta et al., 2019) implies a bulk poros-
473 ity of 54 %, indicating significant microporosity. For Itokawa, average grain density has
474 been estimated based on the modal abundance of minerals in the returned samples, and
475 densities of 3400 kg m^{-3} have been obtained (Tsuchiyama et al., 2011, 2014). This im-
476 plies a bulk porosity of 39 ± 6 % (Abe et al., 2006; Fujiwara et al., 2006; Tsuchiyama
477 et al., 2011), consistent with the results obtained from the mixing theory. For Eros, the
478 power law exponent of $p = 3.31 \pm 0.06$ (Thomas et al., 2001) implies macroporosities

of 40 - 45 %, which is larger than the inferred bulk porosity of Eros. The latter is estimated to be 21-33 % (Yeomans et al., 2000; Wilkison et al., 2002), indicating that macroporosities derived using the presented mixing model are incompatible with the observations. However, although Eros is a heavily fractured body, there is little evidence that it was ever catastrophically disrupted and later reaccumulated into a rubble pile (Wilkison et al., 2002), such that the theory presented here can probably not be be applied.

Results for Ryugu have been obtained assuming minimum and maximum particle sizes of 0.02 m and 140 m, respectively, and these results are robust with respect to the cut-off at small particle sizes $D_{\min}$. Only shifting the cut-off $D_{\min}$ to values larger than 0.30 m has a noticeable effect on the macroporosity. The upper cut-off size $D_{\max}$ was chosen to correspond to the Otohime boulder, which is the largest boulder observed on Ryugu's surface. However, boulders larger than Otohime could potentially reside in Ryugu's interior, which would decrease the obtained macroporosity through a filling of void spaces. Reasonable upper limits on monolith sizes are 200 m, as derived from observations of fast rotators in the asteroid population (Pravec & Harris, 2000) and the catastrophic disruption threshold (Benz & Asphaug, 1999; Jutzi et al., 2010). Assuming $D_{\max} = 200$ m reduces ϕ_{Macro} to 15 %.

One way to increase macroporosity in the above models would be an increased initial porosity in each size bin, which may for example be caused by mechanical interlocking of particles due to particle angularity. For a random loose packing, non-cohesive initial porosity can increase from ∼42 % for smooth frictionless particles to ∼44 % for very rough particles (Onoda & Liniger, 1990; Jerkins et al., 2008). In the frame of the applied mixing model, this effect is taken into account in the chosen initial porosity (Eq. 15), and shifting the applied Gaussian distribution in the performed Monte-Carlo simulations by 2 % results in slightly increased macroporosities of 18.0±3 %. Therefore, while roughness and particle interlocking can increase macroporosity, this is likely not a significant effect.

While the obtained macroporosity may appear to be relatively low, a significant reduction with respect to the porosity of random close packings of monodisperse spheres can be expected. Even binary mixtures of particles can be arranged in packing states with porosities of 15-20 % (Yu & Standish, 1991; Yu et al., 1992), such that it should not be surprising to achieve similar packing densities with the broad size distributions

used here. Ternary mixtures can achieve $\phi_{Macro} < 10$ % (Yu & Standish, 1991), and while most common loose or compact granular materials have macroporosities between 30 % and 50 %, almost any degree of macroporosity between 10 and 90 % can be obtained for polydisperse angular particles (Dullien, 1991). Experimentally, macroporosities down to 10 % have been produced in the lab (Latham et al., 2002). Therefore, the macroporosity of Ryugu obtained here falls within a reasonable range, and Ryugu's high bulk porosity is a direct consequence of the very large microporosity of Ryugu's boulders.

The average grain densities obtained here are much lower than typical grain densities of ordinary chondrites, which range from 3520 to 3710 kg m^{-3} (Flynn et al., 2018), and also lower than those of most carbonaceous chondrites, which typically have grain densities in excess of 3360 kg m^{-3} (Flynn et al., 2018). Only the CM and CI sub-classes show lower grain densities, and $\rho_{CM,Grain} = 2960 \pm 40$ kg m^{-3} while $\rho_{CI,Grain} = 2420$ kg m^{-3} (Consolmagno et al., 2008; Macke et al., 2011; Flynn et al., 2018). The Tagish Lake meteorite, an ungrouped carbonaceous chondrite, exhibits similar grain densities in the range between 2430 and 2840 kg m^{-3} (Ralchenko et al., 2014). While the larger grain densities of 2848 ± 152 kg m^{-3} are consistent with the CM and Tagish Lake results, the lower densities of 2093 ± 95 kg m^{-3} are inconsistent with those of known meteorite samples.

Estimates of grain densities discussed above indicate that extrapolating boulder porosities as a function of thermal conductivity using the model by Flynn et al. (2018) is preferred to extrapolations using the model by Henke et al. (2016). In addition, laboratory measurements of thermal conductivity (Hamm et al., 2019) using the UTPS Tagish Lake meteorite simulant (Miyamoto et al., 2018) provide further evidence of high boulder microporosity. The UTPS simulant has a grain density of 2813 kg m^{-3} and a porosity of 47.5 %, while thermal conductivity was determined to be similar to that of Ryugu's rugged boulders (Hamm et al., 2019). It therefore seems likely that boulder porosity on Ryugu falls within the high range determined by Grott et al. (2019), but more laboratory measurements of thermal conductivity at high porosity are needed to confirm these results and reduce uncertainties. If grain densities are indeed of the order of 2850 kg m^{-3}, Ryugu's bulk porosity is estimated to be 58 % (cf. Eq. 18).

It is noted that close-up images have revealed that many boulders on Ryugu and Bennu exhibit morphologic properties consistent with a brecciated structure (Sugita et al., 2019; Walsh et al., 2019). Breccia would have much larger microporosities than pristine rocks, consistent with the large microporosities preferred here. Furthermore, the presence of breccia on Ryugu and Bennu is consistent with the fact that many carbonaceous chondrites and, in particular, all CM and CI meteorites found on Earth are known to be brecciated (Bischoff et al., 2006). However, it remains to be investigated if brecciation is the main mechanism providing microporosity, or whether the boulder's highly porous structure is a result of the formation mechanisms acting in Ryugu's parent body (Neumann et al., 2014, 2015).

If microporosity in typical carbonaceous asteroids is as high as predicted here for Ryugu, macroporosities of rubble pile asteroids may have been systematically overestimated in the past (e.g., Consolmagno et al., 2008). Macroporosities have been estimated based on measurements of asteroid bulk density and porosities of meteorite samples, the latter of which could have been underestimated compared to values for actual carbonaceous material on asteroids derived from in-situ measurements (Grott et al., 2017, 2019). This bias could be the result of filtering by the Earth's atmosphere, as only the strongest, densest carbonaceous meteoroids would survive atmospheric entry, while weaker samples would break up (Popova et al., 2011). This could explain the absence of high porosity samples in our meteorite collections, where the most porous sample reported to date is the Tagish Lake meteorite, which shows porosities in the range from 26 to 36 % (Ralchenko et al., 2014). The samples to be returned from Ryugu by the Hayabusa2 mission will provide crucial information on this issue.

Results presented here assume that the size-frequency distribution observed on the surface of Ryugu is representative for the entire asteroid, but as discussed in Sec. 1, the reaccretion process itself as well as post accretion surface modifications could influence the observed size-frequency distribution. For example, meteorite impacts could increase the number of small boulders on the surface and the observed size-frequency distribution would be steeper than the distribution in the interior. Therefore, macroporosity would have been overestimated in the presented model, as the interior distribution would move closer to the Fuller minimum (Fuller & Thompson, 1907). Conversely, the Brazil Nut Effect could bias the slope of the surface size-frequency distribution towards smaller values, implying that macroporosity would have been underestimated. This topic can be

addressed once average grain density and possibly also microporosity have been determined from the returned samples, as has been done for Itokawa (Tsuchiyama et al., 2011). Then, Ryugu's macroporosity can be derived given the measured bulk density (Watanabe et al., 2019). Any significant deviation from the macroporosity value calculated here will indicate a non-homogeneous boulder size distribution in the bulk volume of the asteroid.

Acknowledgments

PM. acknowledges funding support from the French space agency CNES, from the European Union's Horizon 2020 research and innovation programme under grant agreement No 870377 (project NEO-MAPP), and from Academies of Excellence: Complex systems and Space, environment, risk and resilience, part of the IDEX JEDI of the Université Côte d'Azur. S.S. acknowledges funding from the JSPS Core-to-Core Program 'International Network of Planetary Sciences.'. W.N. acknowledges support by Klaus Tschira Stiftung. The numerical code and data have been **made available at Figshare: Grott, M. (2020) Supplementary Material for "Macroporosity and Grain Density of Rubble Pile Asteroid (162173) Ryugu.",** `https://doi.org/10.6084/m9.figshare.c.4964363.v3`**.**

References

Abe, S., Mukai, T., Hirata, N., Barnouin-Jha, O., Cheng, A., Demura, H., ... Yoshikawa, M. (2006). Mass and local topography measurements of itokawa by hayabusa. *Science*, *312*(5778), 1344–1347. doi: 10.1126/science.1126272

Arakawa, M., Saiki, T., Wada, K., Ogawa, K., Kadono, T., Shirai, K., ... Miura, A. (2020). An artificial impact on the asteroid 162173 Ryugu formed a crater in the gravity-dominated regime. *Science*, *367*, aaz1701. doi: 10.1126/science.aaz1701

Benz, W., & Asphaug, E. (1999). Catastrophic disruptions revisited. *Icarus*, *142*(1), 5 - 20. doi: 10.1006/icar.1999.6204

Bischoff, A., Scott, E., Metzler, K., & Goodrich, C. (2006). Nature and origins of meteoritic breccias. *Meteorites and the early solar system II*, 679-712.

Britt, D., & Consolmagno S.J., G. (2001). Modeling the Structure of High Porosity Asteroids. *Icarus*, *152*(1), 134-139. doi: 10.1006/icar.2001.6628

Britt, D., Yeomans, D., Housen, K., & Consolmagno, G. (2002). Asteroid density,

porosity, and structure. In (p. 485-500). in: Asteroids III, W. F. Bottke Jr., A. Cellino, P. Paolicchi, and R. P. Binzel (eds), University of Arizona Press, Tucson.

Brown, W., & Wohletz, K. (1995). Derivation of the weibull distribution based on physical principles and its connection to the rosin-–rammler and lognormal distributions. *Journal of Applied Physics*, *78*(4), 2758-2763. doi: 10.1063/1.360073

Consolmagno, G., Britt, D., & Macke, R. (2008). The significance of meteorite density and porosity. *Chemie der Erde-Geochemistry*, *68*(1), 1–29.

Dullien, F. (1991). *Porous media - fluid transport and pore structure (second edition)* (Second Edition ed.). San Diego: San Diego, Academic Press. doi: 10.1016/B978-0-12-223651-8.50006-7

Durda, D., Bagatin, A., Alemañ, R., Flynn, G., Strait, M., Clayton, A., & Patmore, E. (2015). The shapes of fragments from catastrophic disruption events: Effects of target shape and impact speed. *Planetary and Space Science*, *107*, 77 - 83. (VIII Workshop on Catastrophic Disruption in the Solar System) doi: https://doi.org/10.1016/j.pss.2014.10.006

Flynn, G., Consolmagno, G., Brown, P., & Macke, R. (2018). Physical properties of the stone meteorites: Implications for the properties of their parent bodies. *Chemie der Erde / Geochemistry*, *78*(3), 269-298. doi: 10.1016/j.chemer.2017.04.002

Fujiwara, A., Kawaguchi, J., Yeomans, D. K., & et al. (2006). The Rubble-Pile Asteroid Itokawa as Observed by Hayabusa. *Science*, *312*(5778), 1330-1334. doi: 10.1126/science.1125841

Fuller, W., & Thompson, S. (1907). The laws of proportioning concrete. *Trans. Am. Soc. Civ. Eng.*, *59*(2), 67-143.

Graton, L. C., & Fraser, H. J. (1935, December). Systematic Packing of Spheres: With Particular Relation to Porosity and Permeability. *Journal of Geology*, *43*(8), 785-909. doi: 10.1086/624386

Grott, M., Knollenberg, J., Borgs, B., Hänschke, F., Kessler, E., Helbert, J., ... Müller, N. (2017). The MASCOT Radiometer MARA for the Hayabusa 2 Mission. *Space Science Reviews*, *208*(1-4), 413-431. doi: 10.1007/s11214-016-0272-1

Grott, M., Knollenberg, J., Hamm, M., Ogawa, K., Jaumann, R., Otto, K. A., ... Moussi-Soffys, A. (2019). Low thermal conductivity boulder with high porosity identified on C-type asteroid (162173) Ryugu. *Nature Astronomy*, 406. doi:

10.1038/s41550-019-0832-x

Hamm, M., Grott, M., Knollenberg, J., Miyamoto, H., Biele, J., Hagermann, A., ... Zolensky, M. (2019). Thermal Conductivity and Porosity of Ryugu's Boulders from In-Situ Measurements of MARA - the MASCOT Radiometer. In *Lunar and planetary science conference* (p. 1373).

Hamm, M., Pelivan, I., Grott, M., & de Wiljes, J. (2020). Thermophysical modelling and parameter estimation of small Solar system bodies via data assimilation. *Monthl. Not. Roy. Astr. Soc.*, *496*(3), 2776-2785. doi: 10.1093/mnras/staa1755

Henke, S., Gail, H.-P., & Trieloff, M. (2016). Thermal evolution and sintering of chondritic planetesimals. III. Modelling the heat conductivity of porous chondrite material. *Astronomy and Astrophysics*, *589*, A41. doi: 10.1051/0004-6361/201527687

Jerkins, M., Schröter, M., Swinney, H., Senden, T., Saadatfar, M., & Aste, T. (2008). Onset of Mechanical Stability in Random Packings of Frictional Spheres. *Phys. Rev. Lett.*, *101*(1), 018301. doi: 10.1103/PhysRevLett.101.018301

Jutzi, M., Michel, P., Benz, W., & Richardson, D. (2010). Fragment properties at the catastrophic disruption threshold: The effect of the parent body's internal structure. *Icarus*, *207*(1), 54 - 65. doi: 10.1016/j.icarus.2009.11.016

Kameda, S., Suzuki, H., Takamatsu, T., Cho, Y., Yasuda, T., Yamada, M., ... Sugita, S. (2017). Preflight Calibration Test Results for Optical Navigation Camera Telescope (ONC-T) Onboard the Hayabusa2 Spacecraft. *Space Science Reviews*, *208*(1-4), 17-31. doi: 10.1007/s11214-015-0227-y

Kitazato, K., Milliken, R., & Iwata, e. a., T. (2019). The surface composition of asteroid 162173 ryugu from hayabusa2 near-infrared spectroscopy. *Science*, *364*(6437), 272–275. doi: 10.1126/science.aav7432

Kiuchi, M., & Nakamura, A. (2015). Corrigendum to "Relationship between regolith particle size and porosity on small bodies" [Icarus 239 (2014) 291-293]. *Icarus*, *248*, 221-221. doi: 10.1016/j.icarus.2014.10.039

Kiuchi, M., & Nakamura, A. (2015b). Corrigendum to"relationship between regolith particle size and porosity on small bodies"[icarus 239 (2014) 291-293]. *Icarus*, *248*, 221-221.

Krumbein, W. (1941). Measurement and geological significance of shape and roundness of sedimentary particles. *Journal of Sedimentary Petrology*, *11*, 64-72.

672 Latham, J., Munjiza, A., & Lu, Y. (2002). On the prediction of void porosity and
673 packing of rock particulates. *Powder Technology*, *125*, 10-27. doi: 10.1016/S0032
674 -5910(01)00493-4
675 Lauretta, D., Dellagiustina, D., Bennett, C., & et al. (2019). The unexpected sur-
676 face of asteroid (101955) Bennu. *Nature*, *568*(7750), 55-60. doi: 10.1038/s41586
677 -019-1033-6
678 Macke, R., Consolmagno, G., & Britt, D. (2011). Density, porosity, and magnetic
679 susceptibility of carbonaceous chondrites. *Meteorit. Planet. Sci.*, *46*, 1842–1862.
680 Maurel, C., Ballouz, R.-L., Richardson, D., Michel, P., & Schwartz, S. (2017).
681 Numerical simulations of oscillation-driven regolith motion: Brazil-nut effect.
682 *Monthly Notices of the Royal Astronomical Society*, *464*(3), 2866-2881. doi:
683 10.1093/mnras/stw2641
684 Mazrouei, S., Daly, M. G., Barnouin, O. S., Ernst, C. M., & DeSouza, I. (2014).
685 Block distributions on Itokawa. *Icarus*, *229*, 181-189. doi: 10.1016/j.icarus.2013.11
686 .010
687 Michel, P., Ballouz, R.-L., Barnouin, O., Jutzi, M., Walsh, K., May, B., ... Lau-
688 retta, D. (2020). Collisional formation of top-shaped asteroids and implications
689 for the origins of ryugu and bennu. *Nature Communications*.
690 Michel, P., & Richardson, D. (2013). Collision and gravitational reaccumulation:
691 Possible formation mechanism of the asteroid itokawa. *Astron. Astrophys.*, *554*,
692 L1-L4.
693 Michikami, T., Hagermann, A., Kadokawa, T., Yoshida, A., Shimada, A., Hasegawa,
694 S., & Tsuchiyama, A. (2016). Fragment shapes in impact experiments rang-
695 ing from cratering to catastrophic disruption. *Icarus*, *264*, 316-330. doi:
696 10.1016/j.icarus.2015.09.038
697 Michikami, T., Honda, C., Miyamoto, H., & et al. (2019). Boulder size and shape
698 distributions on asteroid ryugu. *Icarus*, *331*, 179 - 191. doi: https://doi.org/10
699 .1016/j.icarus.2019.05.019
700 Michikami, T., Nakamura, A., Hirata, N., Gaskell, R., Nakamura, R., Honda, T.,
701 ... Miyamoto, H. (2008). Size-frequency statistics of boulders on global sur-
702 face of asteroid 25143 Itokawa. *Earth, Planets, and Space*, *60*, 13-20. doi:
703 10.1186/BF03352757
704 Miyamoto, H., Niihara, T., Wada, K., Ogawa, K., Baresi, N., Abell, P., ... Naka-

mura, T. (2018). Phobos Environment Model and Regolith Simulant for MMX Mission. In *Lunar and planetary science conference* (p. 1882).

Nakamura, A., & Fujiwara, A. (1991). Velocity distribution of fragments formed in a simulated collisional disruption. *Icarus*, *92*(1), 132-146. doi: 10.1016/0019-1035(91)90040-Z

Neumann, W., Breuer, D., & Spohn, T. (2014). Modelling of compaction in planetesimals. *A&A*, *567*, A120. doi: 10.1051/0004-6361/201423648

Neumann, W., Breuer, D., & Spohn, T. (2015). Modelling the internal structure of Ceres: Coupling of accretion with compaction by creep and implications for the water-rock differentiation. *A&A*, *584*, A117. doi: 10.1051/0004-6361/201527083

Nishiyama, G., Kawamura, T., Namiki, N., Fernando, B., Leng, K., Saiki, T., ... Arakawa, M. (2020). An Absence of Seismic Shaking on Ryugu Induced by the Impact Experiment on the Hayabusa2 Mission. In *Lunar and planetary science conference* (p. 1806).

Okada, T., Fukuhara, T., Tanaka, S., & et al. (2020). Highly porous nature of a primitive asteroid revealed by thermal imaging. *Natureh*, *579*, 518–52. doi: 10.1038/s41586-020-2102-6

Onoda, G., & Liniger, E. (1990). Random loose packings of uniform spheres and the dilatancy onset. *Phys. Rev. Lett.*, *64*(22), 2727-2730. doi: 10.1103/PhysRevLett.64.2727

Perko, H., Nelson, J., & Sadeh, W. (2001). Surface cleanliness effect on lunar soil shear strength. *J. Geotech. Geoenviron. Eng.*, *127*(4), 371-383. doi: 10.1061/(asce)1090-0241(2001)127:4(371)

Popova, O., Borovicka, J., Hartmann, W., Spurny, P., Gnos, E., Nemtchinov, I., & Trigo-Rodriguiz, J. (2011). Very low strengths of interplanetary meteoroids and small asteroids. *Meteoritics & Planetary Science*, *46*(10), 1525-1550. doi: 10.1111/j.1945-5100.2011.01247.x

Powers, M. (1953). A new roundness scale for sedimentary particles. *Journal of Sedimentary Research*, *23*(2), 117-119. doi: 10.1306/D4269567-2B26-11D7-8648000102C1865D

Pravec, P., & Harris, A. (2000). Fast and Slow Rotation of Asteroids. *Icarus*, *148*, 12-20. doi: 10.1006/icar.2000.6482

Ralchenko, M., Britt, D. T., Samson, C., Herd, C. D. K., Herd, R. K., & McCaus-

land, P. J. A. (2014). Bulk Physical Properties of the Tagish Lake Meteorite Frozen Pristine Fragments. In *Lunar and planetary science conference* (p. 1021).

Riley, N. (1941). Projection sphericity. *J. Sediment. Petrol.*, *11*, 94-95.

Rosin, E., P.and Rammler. (1933). The laws governing the fineness of powdered coal. *Journal of the Institute of Fuel*, *7*, 29–36.

Scheeres, D. J., Hartzell, C. M., Sánchez, P., & Swift, M. (2010). Scaling forces to asteroid surfaces: The role of cohesion. *Icarus*, *210*(2), 968-984. doi: 10.1016/j.icarus.2010.07.009

Schröder, S. E., Carsenty, U., Hauber, E., Schulzeck, F., Raymond, C. A., & Russell, C. T. (2020, September). The boulder population of asteroid 4 Vesta: Size-frequency distribution and survival time. *arXiv e-prints*, arXiv:2009.00957.

Scott, G. (1960). Packing of spheres: Packing of equal spheres. *Nature*, *188*, 908–909. doi: 10.1038/188908a0

Sugita, S., Honda, R., Morota, T., & et al. (2019). The geomorphology, color, and thermal properties of ryugu: Implications for parent-body processes. *Science*, *364*(6437). doi: 10.1126/science.aaw0422

Suzuki, H., Yamada, M., Kouyama, T., Tatsumi, E., Kameda, S., Honda, R., ... Sugita, S. (2018). Initial inflight calibration for hayabusa2 optical navigation camera (onc) for science observations of asteroid ryugu. *Icarus*, *300*, 341 - 359. doi: https://doi.org/10.1016/j.icarus.2017.09.011

Tancredi, G., Roland, S., & Bruzzone, S. (2015). Distribution of boulders and the gravity potential on asteroid Itokawa. *Icarus*, *247*, 279-290. doi: 10.1016/j.icarus.2014.10.011

Tatsumi, E., Kouyama, T., Suzuki, H., Yamada, M., Sakatani, N., Kameda, S., ... Sugita, S. (2019). Updated inflight calibration of hayabusa2's optical navigation camera (onc) for scientific observations during the cruise phase. *Icarus*, *325*, 153 - 195.

Thomas, P. C., Veverka, J., Robinson, M. S., & Murchie, S. (2001). Shoemaker crater as the source of most ejecta blocks on the asteroid 433 Eros. *Nature*, *413*(6854), 394-396. doi: 10.1038/35096513

Tsuchiyama, A., Uesugi, M., Matsushima, T., Michikami, T., Kadono, T., Nakamura, T., ... Kawaguchi, J. (2011). Three-dimensional structure of hayabusa samples: Origin and evolution of itokawa regolith. *Science*, *333*(6046), 1125–1128.

771 doi: 10.1126/science.1207807

772 Tsuchiyama, A., Uesugi, M., Uesugi, K., Nakano, T., Noguchi, R., Matsumoto, T.,
773 ... Fujimura, A. (2014). Three-dimensional microstructure of samples recovered
774 from asteroid 25143 itokawa: Comparison with ll5 and ll6 chondrite particles.
775 *Meteoritics & Planetary Science*, *49*(2), 172-187. doi: 10.1111/maps.12177

776 Wadell, H. (1932). Volume, Shape, and Roundness of Rock Particles. *Journal of Ge-*
777 *ology*, *40*(5), 443-451. doi: 10.1086/623964

778 Walsh, K. J., Jawin, E. R., Ballouz, R. L., Barnouin, O. S., Bierhaus, E. B., Con-
779 nolly, H. C., ... Osiris-Rex Team (2019). Craters, boulders and regolith of
780 (101955) Bennu indicative of an old and dynamic surface. *Nature Geoscience*,
781 *12*(4), 242-246. doi: 10.1038/s41561-019-0326-6

782 Watanabe, S., Hirabayashi, M., Hirata, N., & et al. (2019). Hayabusa2 arrives at the
783 carbonaceous asteroid 162173 ryugu—a spinning top–shaped rubble pile. *Science*,
784 *364*(6437), 268–272. doi: 10.1126/science.aav8032

785 Weibull, W. (1951). A statistical distribution function of wide applicability. *J. Appl.*
786 *Mech.-Trans. ASME*, *18 (3)*, 293–29.

787 Wilkison, S., Robinson, M., Thomas, P., Veverka, J., McCoy, T., Murchie, S., ...
788 Yeomans, D. (2002). An estimate of eros's porosity and implications for internal
789 structure. *Icarus*, *155*(1), 94 - 103. doi: https://doi.org/10.1006/icar.2001.6751

790 Wilson, L., Keil, K., & Love, S. (1999). The internal structures and densities of as-
791 teroids. *Meteoritics and Planetary Science*, *34*(3), 479-483. doi: 10.1111/j.1945
792 -5100.1999.tb01355.x

793 Wingo, D. (1989). The left-truncated weibull distribution: theory and computation.
794 *Statistical papers*, *30*(1), 39–48.

795 Wood, S. (2020). A mechanistic model for the thermal conductivity of planetary
796 regolith: 1. the effects of particle shape, composition, cohesion, and compression
797 at depth. *Icarus*, *352*, 113964. doi: https://doi.org/10.1016/j.icarus.2020.113964

798 Yamamoto, K., Otsubo, T., Matsumoto, K., Noda, H., Namiki, N., Takeuchi, H.,
799 ... Tsuda, Y. (2020). Dynamic precise orbit determination of Hayabusa2 using
800 laser altimeter (LIDAR) and image tracking data sets. *Earth, Planets, and Space*,
801 *72*(1), 85. doi: 10.1186/s40623-020-01213-2

802 Yasui, M., Yamamoto, Y., Arakawa, M., Hasegawa, S., Sugimura, R., & Yokota, Y.
803 (2019). Impact experiments on granular targets with size frequency distribution

similar to asteroid 162173 Ryugu. In *Epsc-dps joint meeting 2019* (Vol. 2019).

Yeomans, D. K., Antreasian, P. G., Barriot, J. P., Chesley, S. R., Dunham, D. W., Farquhar, R. W., ... Williams, B. G. (2000, September). Radio Science Results During the NEAR-Shoemaker Spacecraft Rendezvous with Eros. *Science*, *289*(5487), 2085-2088. doi: 10.1126/science.289.5487.2085

Yu, A., Bridgwater, J., & Burbidge, A. (1997). On the modelling of the packing of fine particles. *Powder Technology*, *92*(3), 185 - 194. doi: 10.1016/S0032-5910(97)03219-1

Yu, A., & Zou, R. (1998). Prediction of the porosity of particle mixtures. *KONA Powder and Particle Journal*, *16*, 68-81. doi: 10.14356/kona.1998010

Yu, A., Zou, R., & Standish, N. (1992). Packing of ternary mixtures of nonspherical particles. *Journal of the American Ceramic Society*, *75*(10), 2765-2772. doi: 10.1111/j.1151-2916.1992.tb05502.x

Yu, A. B., & Standish, N. (1991). Estimation of the porosity of particle mixtures by a linear-mixture packing model. *Industrial & Engineering Chemistry Research*, *30*(6), 1372-1385. doi: 10.1021/ie00054a045

Zou, R., Gan, M., & Yu, A. (2011). Prediction of the porosity of multi-component mixtures of cohesive and non-cohesive particles. *Chemical Engineering Science*, *66*(20), 4711-4721. doi: 10.1016/j.ces.2011.06.037

Zou, R., & Yu, A. (1996). Evaluation of the packing characteristics of mono-sized non-spherical particles. *Powder Technology*, *88*(1), 71 - 79. doi: https://doi.org/10.1016/0032-5910(96)03106-3